Session 3P3
Devices and Circuits

Application of Finite Network Theory to the Transient Process of Electromagnetic Forming

A. Farschtschi[1], T. Richter[1], and H.-J. Roscher[2]
[1]**Chemnitz University of Technology, Germany**
[2]**Fraunhofer Institute IWU, Germany**

Abstract—Electromagnetic forming typically consists of a coil in front of a workpiece. The discharging of a large capacitor connected to the coil induces eddy currents in the workpiece. The discharging process is simulated by the finite network theory (FNM) for non-magnetic materials. A comparison with the commercial FE program ANSYS is made to verify FNM. Since FNM excludes air from calculation the evaluation results in a relatively small system of differential equations which allows a much faster calculation of the transient compared to ANSYS.

1. Introduction

In recent times efforts are made in workpiece forming using magnetic repulsion forces. The so-called electromagnetic forming (EMF) is usually composed of a coil connected to a large capacitor and a workpiece in front of the coil. The discharging of the capacitor-coil network induces large eddy currents in the workpiece resulting in a perpendicular repulsion force. The aim of the authors is the calculation of an example problem with non-magnetic materials using the finite network theory ([1–4]). Roughly speaking, the finite network theory (FNM) uses inductive coupled resistor networks to create the system of differential equations of current loops whereas most of common FE programs use the magnetic vector potential and the electric scalar potential on finite element nodes as unknowns. FNM results in a relatively small system of differential equations compared to commercial FE programs such as ANSYS. In all calculations the authors used ANSYS as reference FE program to proof the calculations made by FNM. It can be shown that the calculation of the transient of the EMF process is much faster using FNM than the calculation in ANSYS:

1. FNM holds a lower number of degrees of freedom compared to ANSYS.
2. In the case of low-resistivity conductors (coil and workpiece) the transient process in FNM can be calculated by standard methods to solve the related system of differential equations.
3. Once the inverse of the impedance matrix is calculated in FNM only back substitution is necessary in every time step.

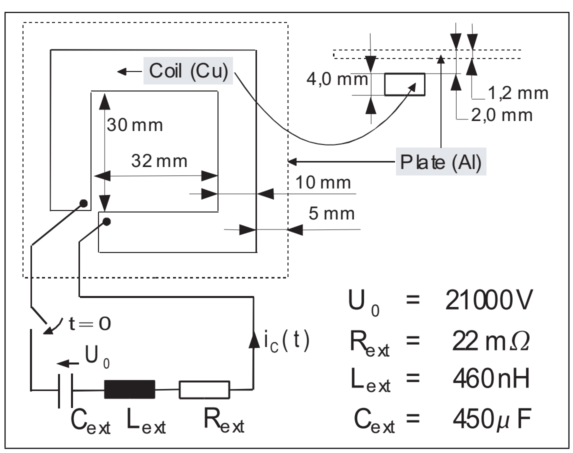

Figure 1: Geometry of example problem and external circuit.

Our example consists of an rectangular single-loop coil made of copper in front of an aluminum plate (see Fig. 1). The external network consists of an external inductance, an external resistor and a capacitor connected to the rectangular coil. The external network provides an additional single loop electric network to the problem called main loop.

2. Simulation of the Transient by the Use of FNM

FNM discretises the conductive volumes of the coil and the aluminum workpiece into rectangular resistor elements i and j with cross sections q_i and q_j and an the lengths l_i and l_j. The self and mutual inductances of resistor elements can be calculated by equation (1):

$$L_{i,j} = \frac{\mu_0}{4\pi}\frac{1}{q_i q_j}\int_{q_i}\int_{q_j}\int_{l_i}\int_{l_j}\frac{\mathrm{d}q_i\mathrm{d}q_j\mathrm{d}l_i\mathrm{d}l_j}{|\vec{r}_i-\vec{r}_j|} \tag{1}$$

Since the network equations are formulated in terms of the mesh current method the self inductances $M_{\xi,\xi}$ and mutual inductances $M_{\xi,\eta}$, $\xi \neq \eta$ of (2) result from a summation of inductances $L_{i,j}$ of (1) over closed current loops C_ξ and C_η:

$$M_{\xi,\eta} = \sum_{i\,(C_\xi)}\ \sum_{j\,(C_\eta)} L_{i,j}\cdot\vec{e}_i\cdot\vec{e}_j \tag{2}$$

The inductances $L_{i,j}$ vanish for perpendicular resistor elements. Since our method uses loop inductances the orientations $\vec{e}_i$ of resistor elements are treated in (2) for simplicity. The $\vec{e}_i$ are parallel to the current flow of a single resistor and include the orientation of a resistor with respect to the loop orientation by sign. The summation $\sum_{i\,(C_\xi)}$ of (2) indicates the summation of all elements i contained in the closed loop C_ξ. The $R_{\xi,\xi}$ of matrix $\mathbf{R}$ in (3) are closed loop resistances. In the case $\xi \neq \eta$ the value $R_{\xi,\eta}$ is the resistance of common branches of the loops C_ξ and C_η with respect to the orientation. $R_{\xi,\eta}=0, \xi\neq\eta$ is fulfilled if two loops don't share common branches. FNM results in a 1st order system of differential equations with the matrices $\mathbf{M}$ and $\mathbf{R}$:

$$\begin{aligned}
\mathbf{M} &= \begin{bmatrix} M_{1,1} & \cdots & M_{1,n} \\ \vdots & & \vdots \\ M_{k+1,1} & \cdots & M_{n,n} \\ M_{n,1} & \cdots & \tilde{M}_{n,n} \end{bmatrix} \\
\mathbf{R} &= \begin{bmatrix} R_{1,1} & \cdots & R_{1,n} \\ \vdots & & \vdots \\ R_{n-1,1} & \cdots & R_{n-1,n} \\ & & \\ R_{n,1} & \cdots & \tilde{R}_{n,n} \end{bmatrix} \\
\tilde{R}_{n,n} &= R_{n,n} + R_{ext} \\
\tilde{L}_{n,n} &= L_{n,n} + L_{ext}
\end{aligned} \tag{3}$$

The external circuit of Fig. 1 enforces the correction of its loop (number n) by the external impedance L_{ext} and the serial resistor R_{ext}. The 1st order system of differential equations is:

$$\begin{aligned}
\mathbf{i}^{(m)}(t) &= \left(\ \mathbf{i}_1^{(m)}(t),\ldots,\ \mathbf{i}_n^{(m)}(t)\ \right)^T \\
\mathbf{u}(t) &= (\ 0,\ldots,\ u_C(t)\ )^T \\
\frac{\mathrm{d}}{\mathrm{d}t}\mathbf{i}^{(m)}(t) &= \mathbf{M}^{-1}\cdot\left[\ \mathbf{u}(t)-\mathbf{R}\cdot\mathbf{i}^{(m)}(t)\ \right] \\
\frac{\mathrm{d}}{\mathrm{d}t}u_C(t) &= -\frac{1}{C_{ext}}\cdot\imath_n^{(m)}(t)
\end{aligned} \tag{4}$$

For the solution of (4) ANSYS offers the implicit Euler method [6]. To make our transient calculation comparable with ANSYS we choose an approximate implementation of the implicit Euler method:

$$\mathbf{y}(t) = \left(\ \imath_1^{(m)}(t),\ldots,\ \imath_n^{(m)}(t),\ u_C(t)\ \right)^T$$

$$\frac{\mathrm{d}}{\mathrm{d}t}\mathbf{y}(t) = \mathbf{A}\cdot\mathbf{y} \tag{5}$$

$$\mathbf{y}_{\nu+1}^{(0)} = \mathbf{y}_\nu + \Delta t\cdot\mathbf{A}\cdot\mathbf{y}_\nu \tag{6}$$

$$\mathbf{y}_{\nu+1} = \mathbf{y}_\nu + \Delta t\cdot\mathbf{A}\cdot\mathbf{y}_{\nu+1}^{(0)} \tag{7}$$

During step $\nu \rightarrow \nu + 1$ of the transient an estimation of the new solution vector $\mathbf{y}_{\nu+1}^{(0)}$ is calculated by the explicit Euler method [5], see equation (6) and algorithm 1. By the use of $\mathbf{y}_{\nu+1}^{(0)}$ a second application of the explicit Euler method in (7) results in an approximation of the implicit Euler method.

Equations (6) and (7) are calculated by the Cholesky decomposition of $\mathbf{M} = \mathbf{B}_L \cdot \mathbf{B}_L^T$ of the inductance matrix $\mathbf{M}$ instead of the use of the system matrix $\mathbf{A}$ of the general form of a linear system of differential equations (6). The algorithm of equation (6) is:

Algorithm 1 Single step of explicit Euler method

1: Back substitution for vector $\mathbf{x}$
$\mathbf{B}_L \cdot \mathbf{x} = \mathbf{u}_\nu - \mathbf{R} \cdot \mathbf{i}_\nu^{(m)}$
2: Back substitution for vector $\mathbf{y}$
$\mathbf{B}_L^T \cdot \mathbf{z} = \mathbf{x}$
3: $\mathbf{i}_{\nu+1}^{(m)} = \mathbf{i}_\nu^{(m)} + \Delta t \cdot \mathbf{z}$
4: $u_{C,\nu+1} = u_{C,\nu} - \Delta t \cdot \frac{1}{C_{ext}} \cdot i_{n,\nu}^{(m)}(t)$

3. Numerical Results

The discharging of the capacitor of the example problem was calculated by FNM and ANSYS. In both cases the same discretisation of the aluminum plate (20 × 20 × 3 elements) and of the coil (3 × 4 elements for height and width of cross section, 3 mm discretisation for length) was used. Fig. 2 shows the discretisation of FNM including the main loop containing the external circuit and a cutout of the finite element discretisation of ANSYS. In ANSYS we used SOLID97 and INFIN111 elements (see Tab. 1).

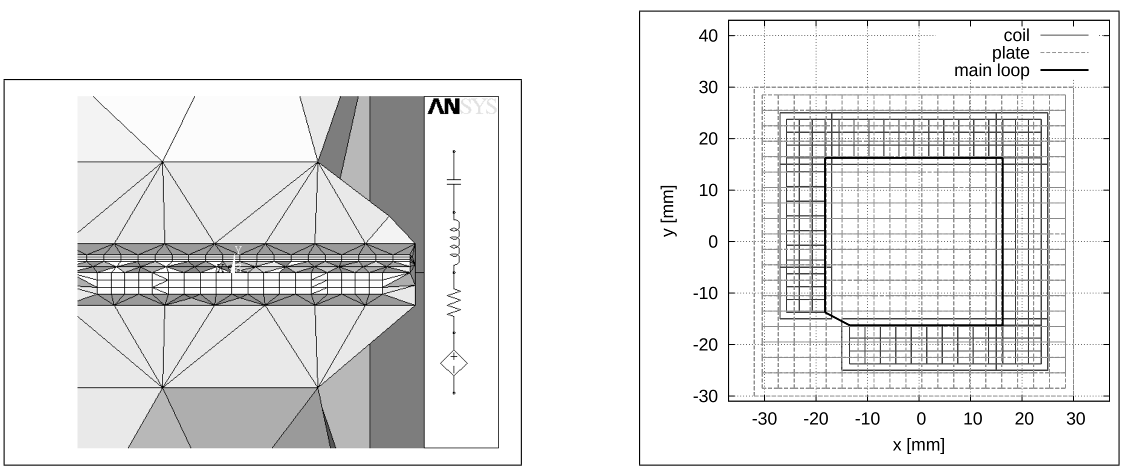

(a) (b)

Figure 2: Discretisation of ANSYS (a) and finite network theory (b).

Table 1: ANSYS discretisation and degrees of freedom (DOF).

Area	*Type*	*Number of FE*
Coil	SOLID97,4,0	636
Plate	SOLID97,1,0	1200
Air	SOLID97,0,0	9584
Infinite area	INFIN111,1	130
DOF		16834

Since FNM excludes air from calculation this method results in a system of differential equations with significantly smaller degrees of freedom of about 1/6 compared to ANSYS (see Tab. 2). Once the Cholesky decomposition of the inductance matrix is calculated, the application of the Euler method in FNM for the evaluation of the transient process is straight forward. Our ANSYS version provides for transient calculations of electromagnetic-circuit coupled fields only a direct standard solver [6]. In connection with the higher number of degrees of freedom the total computing time in ANSYS is about 80 times the computing time of FNM for an 83-point transient (see Tab. 3). A more appropriate solver of the transient calculation could improve the total computing time in ANSYS. Despite this fact efforts of the finite network method (FNM) still remain since FNM results in a system of differential equations with a much lower number of degrees of freedom.

Table 2: FNM discretisation and degrees of freedom (DOF).

Area	*DOF*
Coil	907
Plate	1881
Mesh of external circuit	1
Capacitor of external circuit	1
DOF	2790

Table 3: Comparison of computing time for the 83-point transient simulation.

Method	*Processor*	*Time*
FNM	Mesh generation	127.7 s
	Matrix generation	213.0 s
	Cholesky decomposition	47.7 s
	Transient	129.1 s
	Total time	**8 min 38 s**
ANSYS	Model generation	negligible
	Transient	11 h 38 min
	Total time	**11 h 38 min**

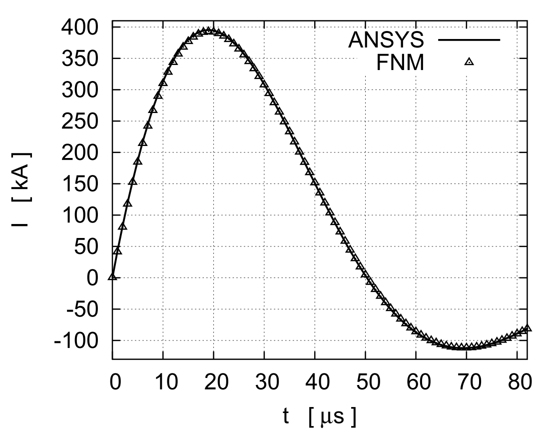

Figure 3: Comparison of the discharging of the external circuit calculated by ANSYS and FNM.

The discharging current of the capacitor is mainly determined by the external current. We calculated the transient with a time step of $1\,\mu$s. Care must be taken on the solution algorithm of linear system of differential equations. There may be deviations of about 10 percent in the peak values of the transient comparing the explicit and implicit Euler method. Fig. 3 depicts that our approximate implementation (6), (7) is in very good agreement with the exact realisation in ANSYS. Furthermore, FNM results in a right evaluation of eddy currents. Fig. 4 shows the total eddy current density on the lower side of the aluminum workpiece facing the copper coil. Smaller deviations are expected: In ANSYS the faces of the single-loop coil are connected to the external circuit whereas in FNM the coil is attached only by single mesh to the external circuit.

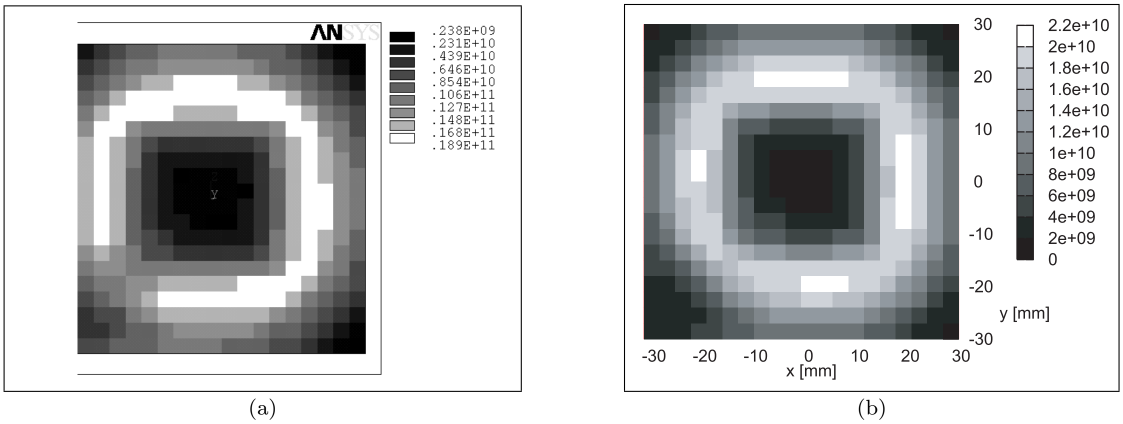

Figure 4: Total eddy current density in $\mathrm{A} \cdot \mathrm{m}^{-2}$ at $t = 20\,\mu s$ calculated by ANSYS (a) and FNM (b). Both figures show the eddy current density on the lower side of the aluminum plate facing the rectangular copper coil. Both models use a discretisation of 3 in height of the workpiece with rectangular elements.

4. Conclusion

The transient calculation of electromagnetic forming can be done by the use of commercial finite element codes or by of the finite network method (FNM). Since the finite network method discretises conducting areas into inductively coupled resistor networks and excludes air from calculation our method results in a system of 1st order differential equations with a significantly smaller number of unknowns. That's why FNM is the preferred method to simulate inductance phenomena of conductors with relatively small volumes embedded in air.

We confirmed our hypothesis by a comparison of ANSYS and FNM. The efforts in computing time of FNM reinforces when a transient simulation is necessary since every time step of the transient requires the solution of an associated linear equation system. A comparison of the absolute value of the eddy currents was made using the same discretisation of the source of the magnetic field and the eddy current domain in both methods (ANSYS and FNM). The good agreement of the distribution of total eddy currents of FNM and the well-known finite element program ANSYS confirms the applicability of FNM to eddy current problems of non-magnetic materials.

REFERENCES

1. Weeks, W. T., L. L. Wu, M. F. McAllister, and A. Singh, "Resistive and inductive skin effect in rectangular conductors", *IBM J. Res. Develop.*, Vol. 23, No. 6, 652–660, 1979.
2. Farschtschi, A., "Dreidimensionale Wirbelstromberechnung nach der Netzwerkmethode," *etz Archiv*, Vol. 8, No. 5, 165–169, 1986.
3. Farschtschi, A. and S. Drechsler, "The Finite Network Method in Different Branches of Field Calculation," *12th Conference on the Computation of Electromagnetic Fields*, Vol. 2, Compumag, Sapporo, Japan, 558-559, October 25–28, 1999.
4. Farschtschi, A. and T. Richter, "A robust preconditioner for GMRES applied to finite network method," *Progress In Electromagnetic Research Symposium 2005*, Hangzhou, China, August 22–26, 2005.
5. Engeln-Muellges, G. and F. Reutter, Numerische Mathematik fuer Ingenieure, BI Wissenschaftsverlag, 1987.
6. *ANSYS User's Manual for Revision 5.0*, Vol. 4, Theory, 17–12.

Tensor Harmonic-balance Analysis of Forced Microwave and Millimeter-wave Circuits

O. P. Paixão and H. E. Hernández-Figueroa
Universidade Estadual de Campinas, Brazil

A novel harmonic balance (HB) simulation [1, 2] framework based on recently developed tensor method for sparse nonlinear equations [3, 4] is presented. This new method bases each iteration on a local, quadratic model where the quadratic term is represented by a rank one tensor object. Like standard Newton's methods, tensor methods are general purpose methods intended especially for problems where the jacobian matrix at the solution is singular or ill-conditioned. In the context of forced HB simulation, this situation may be found in the solution of nonlinear circuits operating near a turning point.

The complexity of forming, storing and solving the tensor model is little compared to the solution of the local linear model required by Newton's methods. The tensor term is selected so that the model interpolates a small number of residuals in the recent history of iterates. The solution of the tensor model leads to an unconstrained optimization problem with dimension equals to the number of iterates used in the interpolation. For an interpolation using one past iterate the optimization reduces to a one-variable problem that can be straightforwardly solved in a closed form. Moreover, numerical experiments have shown that using additional iterates in the interpolation produce only a marginal improvement in the computation performance of the tensor method.

In our implementation of a global tensor method, we utilized a novel curvilinear linesearch technique [5] as globalization strategy. This technique has enticing properties and obviates the need to separately compute an extra linesearch in the Newton direction, as previously required by tensor methods.

To improve the computation performance of the tensor method on weakly nonlinear problems we propose the use of simplified tensor iterations where the jacobian matrix is kept constant. If the jacobian matrix is computed only once, we can develop an extension of the linear-centric modeling approach to HB simulation [6]. This extended ("quadratic-centric") modeling approach uses approximated second-order information and therefore, it is expected to perform better than the conventional approach. The basics of the new approach is illustrated for a simple diode circuit.

Finally, the robustness and computation performance of the proposed tensor-oriented HB simulation tool is verified for a different classes of microwave and millimeter-wave circuits, they are: GaAs MESFET power amplifier, HEMT travelling-wave switch and InP HBT downconverter. Indeed, several numerical results from single-tone (distortion) and two-tone (mixing and intermodulation) analysis are performed in these circuits. These benchmark results clearly shows superior power-handling capabilities and lower execution time our proposed simulator when compared with standard Newton-based HB simulators.

REFERENCES

1. Kundert, K. S. and A. Sangiovanni-Vincentelli, "Simulation of nonlinear circuits in the frequency domain," *IEEE Trans. Computer-Aided Design*, Vol. 5, No. 4, 521–535, Oct. 1986.
2. Rizzoli, V., et al., "State-of-the-art harmonic-balance simulation of forced nonlinear microwave circuits by the piecewise technique," *IEEE Trans. Microwave Theory Tech.*, Vol. 40, No. 1, 12–28, Jan. 1992.
3. Schnabel, R. B. and P. D. Frank, "Tensor methods for nonlinear equations," *SIAM J. Numer. Anal.*, Vol. 21, No. 5, 815–843, Oct. 1984.
4. Bouaricha, A. and R. B. Schnabel, *Tensor Methods for Large, Sparse Systems of Nonlinear Equations*, Tech. Report MCS-P473-1094, Mathematics and Computer Science Division, Argonne National Laboratory, Argonne, IL, USA, 1994.
5. Bader, B. W. and R. B. Schnabel, "Curvilinear linesearch for tensor methods," *SIAM J. Sci. Comput.*, Vol. 25, No. 2, 604–622, 2003.
6. Li, P. and L. Pileggi, "A linear-centric modeling approach to harmonic balance analysis," *Design and Automation in Europe 2002*, 634-639.

Split-Torus Configuration of the Toroidal/Helical Electron-Orbits for High-Power-Microwave Amplifiers

R. A. Speciale
Research and Development Inc., USA

A new, innovative geometry was introduced at PIERS 2004 [1], for the electron trajectories of High-Power Microwave sources, in the form of closed, multi-turn Toroidal/Helical orbits. That new electron trajectory geometry provides many technical advantages, such as a very compact implementation of multi-beam HPM klystrons, elimination of the high-voltage pulsed-source and of the beam-dump, possibility of beam-stacking injection and of beam re-acceleration. The originally introduced geometry of closed, multi-turn Toroidal/Helical orbits introduced in Reference [1] is shown in Fig. 1, with 9 turns shown in blue and 120 electron-bunches shown in red.

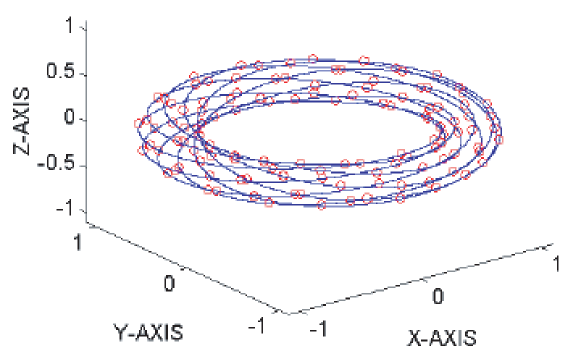

Figure 1: Toroidal/Helical orbits with 120 bunches.

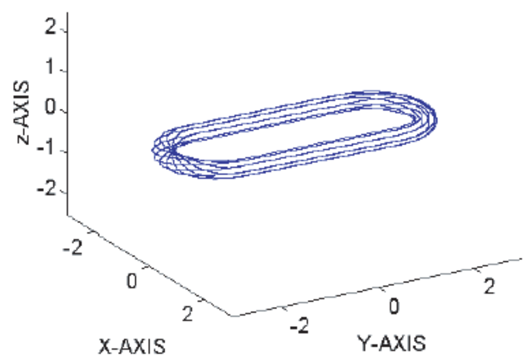

Figure 2: Spli-torus Toroidal/Helical orbit.

An alternate configuration of the closed, multi-turn Toroidal/Helical orbits has now been developed, that provides the possibility of inserting two straight orbit-sections, between the two 180° torus-arcs. That new orbitgeometry provides the possibility of inserting many of the required insertion-devices, such as accelerating and power-extraction microwave-cavities, strong-focusing quadrupole magnetic-lenses, a beam-injection and a beamextraction channels, along the two straight orbit-sections, rather than within the two twisting 180° torus-arcs. The new electron trajectory geometry was obtained by modifying the parametric equations of the original orbit-geometry as required to make both the orbit-curvature and torsion zero along one torus diameter, fom 0° to 180° azimuth.

REFERENCES

1. Speciale, R. A., "High power microwave amplifiers with Toroidal/Helical orbits," *PIERS 2004*, Pisa, Italy.

Exact Expressions of the Orbit-curvature and Curvature-radius of the Toroidal/Helical Orbits

R. A. Speciale
Research & Development Inc., USA

Abstract—Closed-from, exact expressions of the Toroidal/Helical orbit-curvature and curvature-radius, have been obtained by first computing the first and second derivatives of the x, y and z components of the orbit position-vector $\mathbf{r}$ as function of the wrapping-angle $\boldsymbol{\theta}$, and by then substituting those derivatives in the general expression of the curvature of a parametric space-curve in three dimensions. Such closed-form exact expressions open the possibility of computing the value of the continuously-evolving dipole magnetic-field $\boldsymbol{B}$, required to guide an electron-beam of known given energy $\boldsymbol{E}$, expressed in Mev , along the given orbit. Additionally, the maximum and minimum values of the dipole magnetic-field were given by performing preliminary numerical computations with $n = 9$ and $c = 0.2$.

1. Introduction

High power microwave (HPM) sources are almost always designed as vacuum-electronic devices, and are characterized by the capability of generating output powers in the range of Megawatt to Gigawatt, by using beam-voltages of hundreds of kilovolts, and beam-currents of tens of ampere. HPM sources operate in either of three broadly-defined modes: a) Short Pulse, at pulse lengths of 0.1–10 μs, b) Long Pulse, at pulse lengths of 0.1–10 ms, and c) Continuous Wave (CW). The design of high power microwave (HPM) sources has been gradually evolving during at least the past thirty years, primarily stimulated by applications to high energy charged-particle accelerators, and to directed-energy weapons. A number of classic review-papers document that evolution (see [1, 2]). Currently, high energy charged-particle accelerators use almost exclusively high-power klystron amplifiers [3], that attain peak-powers of hundreds of Megawatt in short-pulse operation, tens of Megawatt in long-pulse operation, and about a Megawatt in CW mode. Such amplifiers provide, while converting DC to microwaves, power-efficiency of 50%–60%, and power-gain of 40 dB–60 dB. The electron beam of klystron amplifiers is sharply bunched by *velocity modulation*, followed by a *drift-space* where the accelerated faster electron catch-up with the decelerated slower electron. The so attained sharp bunching generates, upon the continuous-current electron-beam, the required microwave-frequency component, that is the essential source of the generated high-power microwave output.

Quite recently, a number of multi-beam klystrons (MBK) have been developed experimentally, and at least three different MBK models are already commercially available (see [4–8]). Multi-beam klystrons operate at reduced electron-gun voltage, and higher total beam-current than the single-beam designs, thus preventing occasional destructive gun-diode discharges, and increasing the power-efficiency up to $\sim$ 75%. The power-efficiency (measured as the ratio of output microwave power to input DC power) is however still limited, even in MBK, as it is obviously impossible to extract *all* the microwave energy from a sharply-bunched electron-beam, without having the high space-charge-density of the slowing beam force it into uncontrollable defocusing. All high-power klystron amplifiers include therefore a device known as *the beam dump*, which is a high-volume expansion of the klystron vacuum-enclosure, located beyond the microwave-power extraction-structure, where the not-quite completely energy-depleted electron-beam is collected, while converting (*wasting !*) its residual energy to heat *and* X-rays.

2. Toroidal/Helical Orbits

A new, innovative design of High Power Microwave (HPM) Electron-Beam Amplifier was presented by the Author at the PIERS 2004 Symposium, in Pisa, Italy [14]. That new design has the capability of attaining multi-megawatt output power levels, even in long-pulse, high duty cycle or even continuous wave (CW) operation, with very high efficiency, very high spectral-purity, and very low levels of phase and amplitude noise. The new design was initially conceived as a combination of a multi-beam klystron (MBK), with an Electron Storage Ring (ESR). Very high power-efficiency may be attained by having a sharply-bunched High-Current, Relativistic Electron Beam (HIREB) circulate around a *closed*, *re-entrant* multi-turn orbit, within a strong-focusing, alternating-gradient (AG) magnetic field, generated by an azimuth-periodic lattice of beam-guiding magnetic-dipoles, and magnetic quadrupole lenses. High beam currents may then be attained because, by using a multi-turn *helical* electron-beam orbit, running on the outer surface of a virtual torus-surface, the beam current and the space-charge density in each of the individual orbit-turns can be much lower than in a single-turn orbit. That orbit configuration was initially conceived as a way of increasing the power-efficiency of high-power klystron amplifiers, by eliminating *the beam dump*, and by introducing a mechanism of beam-energy recovery, similar to that of Energy-Recovery Linacs (ERL).

It was soon seen however that the use of such closed multi-turn electron-orbit would essentially reduce the foot-print of the newly-conceived device by a factor in the order of the square of the integer number $\boldsymbol{n}$ of turns, while keeping the total orbit length unchanged, relative to that of a single-turn Electron Storage Ring (ESR).

It was also seen that, by keeping the electron-beam energy always in a relativistic range (such as for instance from 50 Mev to 100 Mev), much higher single-turn beam-current, and much higher total stored beam-energy (expressed in Joule) could be attained under a strong-focusing, alternating-gradient (AGS) magnetic field, while at the same time any partial extraction of microwave-energy from the bunched circulating beam would not appreciably change the electron orbital-frequency. Indeed, the total stored beam-energy (expressed in Joule) is obviously stored in the relativistic $(\boldsymbol{\gamma}-1)\,\boldsymbol{m}_0$ mass-increase of the electrons, multiplied by the square of the constant speed of light. Then, by keeping the electron-energy (expressed in Mev) in a relativistic range, very large amounts of microwave energy (expressed in Joule) could be extracted from the circulating sharply-bunched beam, while hardly changing the electron relativistic velocity-factor $\boldsymbol{\beta}$ ($\boldsymbol{\beta}=\sqrt{(\gamma^2-1)/\gamma^2}$, while $\Delta\,\boldsymbol{E}=\Delta\,\gamma\boldsymbol{m}_0\boldsymbol{c}^2$). As a consequence, such partial microwave-power extraction would hardly change the electron orbit-frequency, provided the beam-energy (expressed in Mev) is kept within a relativistic range, where $\boldsymbol{\beta}$ is a very slow function of $\boldsymbol{\gamma}$. In the light of these considerations, the new HPM amplifier design, that was initially conceived as a combination of the multi-beam klystron (MBK) with an Electron-Storage Ring (ESR), actually appears to perform the function of an Energy-Storage Ring (while still being nevertheless an "ESR"). Quite obviously, in any closed-orbit electron-device, the local orbit curvature is a parameter of fundamental significance, as it determines the magnetic-field flux-density required in the beam-steering dipole-magnets, and in the beam-focusing quadrupole lenses, as function of the electron-beam energy (expressed in Mev), and also determines the orbit-frequency of the electron-bunches, by determining the orbit curvature-radius. A closed-form, exact expression of the orbit-curvature, has now been obtained by first computing the first and second derivatives of the $\boldsymbol{x}$, $\boldsymbol{y}$ and $\boldsymbol{z}$ components of the orbit position-vector $\boldsymbol{r}$ as function of the *wrapping-angle* $\boldsymbol{\theta}$, and by then substituting those derivatives in the general expression of the curvature of a parametric space-curve in three dimensions [13].

3. Orbit Equations

The selected *toroidal/helical* orbit-configuration was defined as a parametric space-curve in three dimensional space (R^3), with its Cartesian coordinates being functions of the azimuth-angle $\boldsymbol{\varphi}$ (measured around the torus-axis), and of the *wrapping-angle* $\boldsymbol{\theta}$ (measured around the torus circular cross-section), with the implied condition that the ratio of the two angle periods be rational, such that the orbit closes on itself after an integer number of turns $\boldsymbol{n}$ (for $0\le\boldsymbol{\varphi}\le 2\mathbf{n}\boldsymbol{\pi}$). The parametric equations of that orbit are expressed by:

$$\hat{r}\,(\varphi,\theta)=x\,(\varphi,\theta)\cdot\hat{i}+y\,(\varphi,\theta)\cdot\hat{j}+z\,(\varphi,\theta)\cdot\hat{k} \tag{1}$$

where $\boldsymbol{\varphi}$ is the azimuth angle around the torus-axis, and $\boldsymbol{\theta}$ is the helical *"wrapping angle"* around the torus circular cross-section. The three Cartesian components $\boldsymbol{x}$, $\boldsymbol{y}$ and $\boldsymbol{z}$ of the position-vector $\boldsymbol{r}$, and the linear relation between the angles $\boldsymbol{\varphi}$, and $\boldsymbol{\theta}$ are given by:

$$x = (\,R + r\,\cos\theta\,)\,\cos\varphi \tag{2}$$
$$y = (\,R + r\,\cos\theta\,)\,\sin\varphi \tag{3}$$
$$z = r\,\sin\theta \tag{4}$$
$$\theta = \frac{n-1}{n}\,\varphi \tag{5}$$

A 3D display of the selected Toroidal/Helical orbit configuration is shown in Figure 1, including a 3D display of the locus of the moving curvature center (*the "evolute" !*). A 2D display of the corresponding X–Y plane projections is shown in Figure 2.

4. Curvature

Closed-form expressions have now been obtained for the multi-turn electron-orbit *curvature,* and for the orbit *curvature-radius*, as function of the azimuth-angle $\boldsymbol{\varphi}$, and *wrapping-angle* $\boldsymbol{\theta}$. The general expression of the curvature of a space-curve in 3D is [11]:

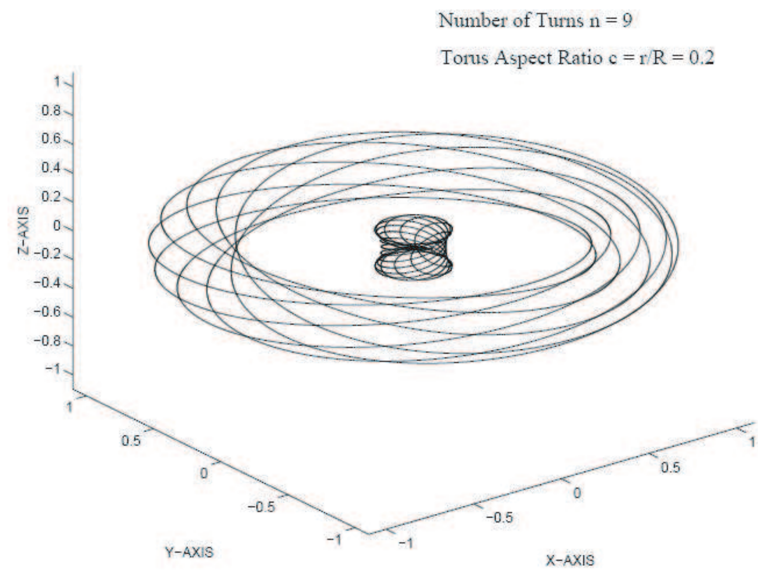

Figure 1: 3D display of the toroidal/helical orbit and of its moving curvature center.

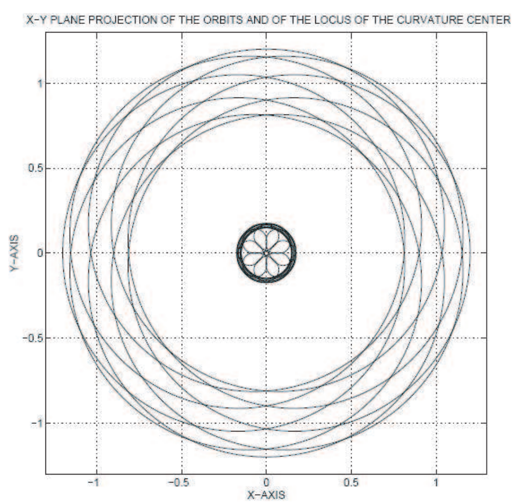

Figure 2: X-Yplane projection of the toroidal/helical orbit and of its moving curvature center.

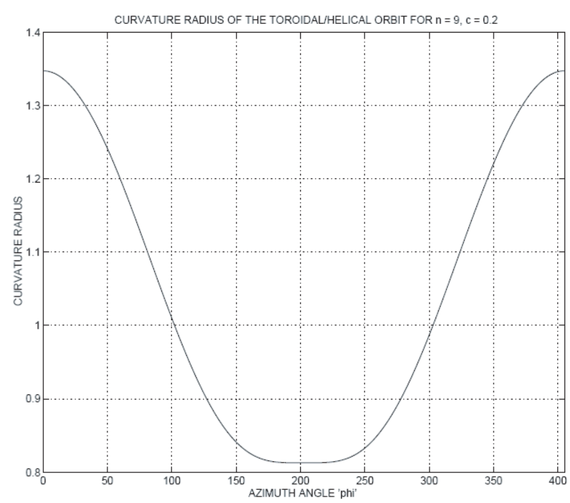

Figure 3: Normalized curvature radius of the toroidal/helical orbit for $n = 9$ and $c = 0.2$.

$$\kappa(\varphi) = \frac{\vec{r'}(\varphi) \times \vec{r''}(\varphi)}{\left\|\vec{r'}(\varphi)\right\|^3} \quad \text{where} \tag{6}$$

$$\vec{r'}(\varphi) = \frac{dx}{d\varphi} \cdot \vec{i} + \frac{dy}{d\varphi} \cdot \vec{j} + \frac{dz}{d\varphi} \cdot \vec{k} \quad \text{and} \tag{7}$$

$$\vec{r''}(\varphi) = \frac{d^2x}{d\varphi^2} \cdot \vec{i} + \frac{d^2y}{d\varphi^2} \cdot \vec{j} + \frac{d^2z}{d\varphi^2} \cdot \vec{k} \tag{8}$$

are the first and second derivatives of the position-vector $\hat{r}(\varphi,\theta) = x(\varphi,\theta)\cdot\hat{i} + y(\varphi,\theta)\cdot\hat{j} + z(\varphi,\theta)\cdot\hat{k}$

The vector-product in the numerator of the general expression (6) is given by:

$$\vec{r}'(\varphi)\times\vec{r}''(\varphi) = \begin{bmatrix} i & j & k \\ \frac{dx}{d\varphi} & \frac{dy}{d\varphi} & \frac{dz}{d\varphi} \\ \frac{d^2x}{d\varphi^2} & \frac{d^2y}{d\varphi^2} & \frac{d^2z}{d\varphi^2} \end{bmatrix} \tag{9}$$

and it expands to:

$$\begin{aligned} \vec{r}'(\varphi)\times\vec{r}''(\varphi) = & \left(\frac{dy}{d\varphi}\frac{d^2z}{d\varphi^2} - \frac{dz}{d\varphi}\frac{d^2y}{d\varphi^2}\right)\cdot\vec{i} \\ & -\left(\frac{dx}{d\varphi}\frac{d^2z}{d\varphi^2} - \frac{dz}{d\varphi}\frac{d^2x}{d\varphi^2}\right)\cdot\vec{j} \\ & +\left(\frac{dx}{d\varphi}\frac{d^2y}{d\varphi^2} - \frac{dy}{d\varphi}\frac{d^2x}{d\varphi^2}\right)\cdot\vec{k} \end{aligned} \tag{10}$$

Further, the cube of the position-vector norm in the denominator of (6) is given by:

$$\left\|\vec{r}'(\varphi)\right\|^3 = \left[\sqrt{\left(\frac{dx}{d\varphi}\right)^2 + \left(\frac{dy}{d\varphi}\right)^2 + \left(\frac{dz}{d\varphi}\right)^2}\right]^3 \tag{11}$$

The actual expression of the Toroidal/Helical orbit-curvature is then obtained by substituting the first and second derivatives of the Cartesian coordinates $\boldsymbol{x}$, $\boldsymbol{y}$, and $\boldsymbol{z}$ in the expressions (7), (8), and (11), and simplified to obtain:

$$\kappa(\varphi) = \frac{\sqrt{\frac{1}{8n^2}\left[k_0 + k_1\cos\left(\frac{n-1}{n}\varphi\right) + k_2\cos\left(2\frac{n-1}{n}\varphi\right) + k_3\cos\left(3\frac{n-1}{n}\varphi\right) + k_4\cos\left(4\frac{n-1}{n}\varphi\right)\right]}}{\left[\sqrt{\left(1+c\cos\theta\right)^2 + c^2\left(\frac{n-1}{n}\right)^2}\right]^3} \tag{12}$$

where the five $\boldsymbol{K}_i$ coefficients are functions of the torus aspect-ratio $\boldsymbol{c}$, and of the number of turns $\boldsymbol{n}$:

$$k_0 = \frac{1}{8n^6}\left\{8n^6 + 4c^2n^2\left\{1+2(n-1)n\left[2+3(n-1)n\right]\right\} + c^4(n-1)^2\left\{8+n\left\{n\left[57+10n(2n-5)\right]\right\}\right\}\right\} \tag{13}$$

$$k_1 = \frac{1}{2n^4}c\left\{3c^2(n-1)^2\left(1+2(n-1)n\right) + 2n^2\left[1+n(3n-2)\right]\right\} \tag{14}$$

$$k_2 = \frac{1}{2n^4}c^2\left\{\left\{2n\left[2+n(2n-3)\right]-1\right\} + (n-1)^2\left[2+n(3n-4)\right]\right\} \tag{15}$$

$$k_3 = \frac{1}{2n^4}c^3(n-1)^2\left[1+2n(n-1)\right] \tag{16}$$

$$k_4 = \frac{1}{8n^4}c^4(n-1)^2(2n-1) \tag{17}$$

while the electron-orbit *curvature-radius* $\boldsymbol{\rho}$ is quite obviously expressed by $\boldsymbol{\rho(\theta)} = \mathbf{1}/\boldsymbol{\kappa(\theta)}$ and is a periodic function of the *wrapping-angle* $\boldsymbol{\theta}$, in the $\mathbf{0} \le \boldsymbol{\theta} \le (\mathbf{n}-\mathbf{1})2\boldsymbol{\pi}$ drange (Figure 3), with period $\mathbf{0} \le \boldsymbol{\theta} \le 2\boldsymbol{\pi}$.

Figure 1 shows a 3D display of a Toroidal/Helical orbit, with $\boldsymbol{n} = 9$ and $\boldsymbol{c} = 0.2$, and includes the locus of its moving curvature-center (the orbit *"evolute" !*), while Figure 2 shows the corresponding projection on the X–Y plane. Finally, Figure 3 shows one period of the orbit curvature-radius for $\mathbf{0} \le \boldsymbol{\theta} \le 2\boldsymbol{\pi}$, normalized to $\boldsymbol{R} = 1$. The closed-form exact expressions of the Toroidal/Helical orbit-curvature, and curvature-radius provide the possibility of computing the value of the continuously-evolving dipole magnetic-field $\boldsymbol{B}$, required to guide an electron-beam of known given energy $\boldsymbol{E}$, expressed in Mev, along the given orbit. Preliminary numerical computations with $\boldsymbol{n} = 9$ and $\boldsymbol{c} = 0.2$ have shown the maximum and minimum values of the dipole magnetic-field to be $\boldsymbol{B}_{MAX}$=4274.66 Gauss, and respectively $\boldsymbol{B}_{MIN}$=2578.4 Gauss, for an electron-energy $\boldsymbol{E}$=150 Mev, and $\boldsymbol{B}_{MAX}$=1434.489 Gauss, and respectively $\boldsymbol{B}_{MIN}$=865.258 Gauss, for an electron-energy $\boldsymbol{E}$=50 Mev. The space-orientation of such dipole field would, however, necessarily need to be also continuously evolving, following the continuous evolution of the Toroidal/Helical orbit *torsion* . The general expression of the orbit-torsion is given by [11]:

$$\tau(\varphi) = \frac{\vec{r'}(\varphi) \times \vec{r''}(\varphi) \cdot \vec{r'''}(\varphi)}{\left\|\vec{r'}(\varphi) \times \vec{r''}(\varphi)\right\|^2}$$

The corresponding closed-form, exact expression for Toroida/Helical orbits will be given in a following report.

5. Conclusions

We proposed closed-from, exact expressions of the Toroidal/Helical orbit-curvature and curvature-radius by first computing the first and second derivatives of the x, y and z components of the orbit position-vector r as function of the wrapping-angle $\boldsymbol{\theta}$, and by then substituting those derivatives in the general expression of the curvature of a parametric space-curve in three dimensions. The closed-form exact expressions provide of the possibility of computing the value of the continuously-evolving dipole magnetic-field $\boldsymbol{B}$, required to guide an electron-beam of known given energy $\boldsymbol{E}$, expressed in Mev , along the given orbit. Also, preliminary numerical computations were performed.

REFERENCES

1. Gold, S. H. and G. S. Nusinovich, "Review of high-power microwave source research," *Rev. Sci. Instrum.*, Vol. 68, No. 11, 3945–3974, November 1997. http://www.ireap.umd.edu/ireap/personnel/publications/RSI 03945.pdf
2. Wilson, P. B., "Development and advances in conventional high power rf systems," SLAC-PUB-95-6957, Stanford Linear Accelerator Center, Stanford University, Stanford, CA 94309 USA, http://www.slac.stanf ord.edu/cgi-wrap/getdoc/slac-pub-6957.pdf.
3. Caryotakis, G., "The klystron: a microwave source of surprising range and endurance," *Phys. Plasmas*, Vol. 5, No. 5, 1590–1598, May 1998. http://www.slac.stanford.edu/cgi-wrap/getdoc/slac-pub-7731.pdf; http://www.slac.stanford.edu/ cgi-wrap/getdoc/slac-pub-8186.ps.gz; http://www.eece.unm.edu/ifis/paper s/MTT.pdf; http://media.wiley.com/*product_data*/excerpt/60/07803600/0780360060.pdf; http://www-project.slac.stanford.edu/ lc/wkshp/snowmass2001/snow/Ch4.pdf.
4. Yano, S. and S. Miyake, "The toshiba E3736 multi-beam klystron," *Proceedings of LINAC 2004*, Lübeck, Germany, Paper THP45, 706–708.
5. Beunas, A., G. Faillon, S. Choroba. S., and A. Gamp, "A high efficiency long pulse multi beam klystron for the tesla linear collider," http://www.cap.bnl.gov/mumu/studyii/ *final_draft*/chapter-14/chapter-14.pdf.
6. Larionov, A., V. Teryaev, S. Matsumoto, and Y. H. Chin, "Design of multi-beam klystron in X-band," *Proceeding of the 27th Linear Accelerator Meeting in Japan*, IEDM, 1986A, 2002. http://lcdev.kek.jp/Conf /LAM27/8P-13.pdf or: http://lcdev.kek.jp/USJ/Paper.JFY98-02.pdf
7. Larionov, A., "Optical system of the powerful multiple beam L-band klystron for linear collider," *Proceedings of RuPAC XIX*, 456–458, Dubna 2004.
8. Jongewaard, E., G. Caryotakis, C. Pearson, R. M. Phillips, D. Spren, and A. Vlieks, "The next linear collider klystron deverlopment program," *XX International Linac Conference*, Monterey, California, Paper THA03, 739–741.
9. Rees, D., "Design of 250-MW CW RF system for APT," 0-7803-4376-X/98/, *IEEE*, 2889–2893, 1998. http://epaper.kek.jp/pac97/papers/pdf/9C003.PDF
10. Rees, D., W. Roybal, and III. J. Bradley, "Collector failures on 350 MHz, 1.2 MW CW lystrons at the low energy demonstration accelerator (LEDA)," *XX International Linac Conference*, Monterey, California, Paper THE12, 998–1000.
11. Dodson, C. T. J., "Mathematics 117: lecture notes for curves and surfaces module," *Department of Mathematics, UMIST*, 1–13, Expressions (28) and (29) at page 6, http://www.ma.umist.ac.uk/kd/ma117/117l n.pdf.
12. Dodson, C. T. J., "Introducing curves," *Department of Mathematics, UMIST*, 1–11, Expressions (25) and (26) at page 9, http://www..ma.umist.ac.uk/kd/curves/curves.pdf.
13. Dodson, C. T. J., "Mathematics 117: lecture notes for curves and surfaces module," *Department of Mathematics, UMIST*, 1–13, Expressions (3) at page 3, http://www.ma.umist.ac.uk/kd/ma117/117ln.pdf.
14. Speciale, R. A. "High power microwave amplifiers with toroidal/helical orbits," *PIERS 2004*, Pisa, Italy.
15. Choroba, S., "The tesla RF system," RF 2003, 2003.

Dual-band/Broadband Circular Polarizers Designed with Cascaded Dielectric Septum Loadings

T.-Y. Huang, **Y.-C. Yu**, and **R.-B. Wu**
National Taiwan University, Taiwan

Abstract—A simple method is presented in this paper for realizing a dielectric septum-loaded type circular polarizer with either dual-band or a single broadband response. Two dielectric septum sections with different dielectric constants and lengths that introduce various phase delay to the x- and y-polarizations of the electric field in the same frequency range are cascaded orthogonally to obtain a dual-band response. A single wideband response can also be achieved if two dielectric septum sections are cascaded in parallel instead. Simulations in Ansoft HFSS show that flatter phase response and wider bandwidth can be obtained by the proposed polarizer comparing to single section ones. Moreover, a dual-band response can only be achieved with a two-section design. Taking advantage of dielectric septum-loaded type circular polarizers, the fabrication error or inaccurate dielectric constants can easily be compensated by adjusting the lengths of dielectric septum sections.

1. Introduction

Circular polarizers have been widely studied and discussed because of the important roles they play in communication systems. Groove- or iris-type circular polarizers [1–2] are robust but require precise fabrication processes. Metal septum-type circular polarizers [3] are easy and effective to design and modify but suffer from large signal reflection. A circular polarizer designed with a dielectric septum loading is proposed [4] with simple design procedure and easy compensation of fabrication error while keeping signal reflection level in an acceptable range. This paper gives a further study on dielectric septum-loaded type circular polarizers by extending its concept to two dielectric septum sections. Two orthogonally cascaded dielectric septum sections lead to a dual-band polarizer while a single wideband design can be achieved with two septum sections cascade in parallel.

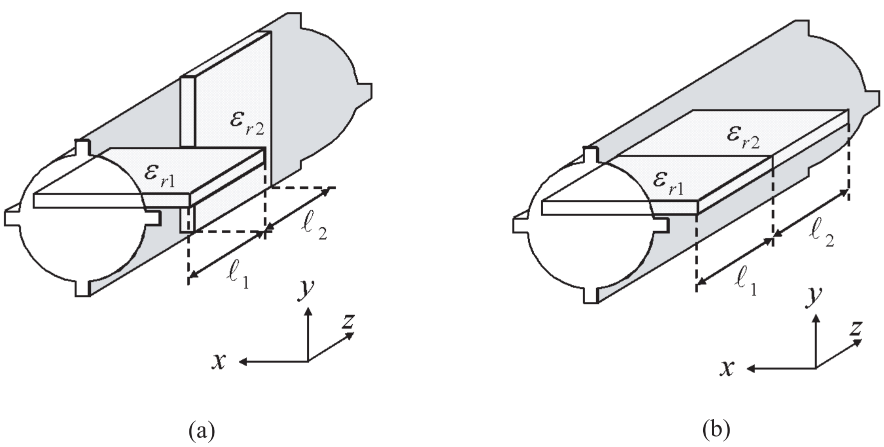

Figure 1: Three dimensional view of the circular polarizer with (a) two orthogonally cascaded septum sections and (b) two septum sections cascaded in parallel.

2. Theory

Figure 1 shows the geometry of the proposed circular polarizers, in which two dielectric septum loadings cascaded either orthogonally (Figure 1(a)) or in parallel (Figure 1(b)) are inserted in the middle of the waveguide. Slots on the waveguide wall are needed for precisely locating the dielectric septum. An incident wave E_0 oriented at 45° relative to the dielectric septum can be decomposed into two equal orthogonal projections as shown in Figure 2(a). These two components will propagate through the septum regions with different propagation constants. The electric field component which is in parallel with the septum is strongly perturbs. As a result the effective dielectric constant for this component is greater and vice versa. If the relative dielectric constants and the lengths of these two septum regions are allowed to be different, various phase differences between the two field components will be introduced by the two septum regions in the same frequency range, as shown in Figure 2(b). If these parameters are chosen properly, a dual-band circular polarizer as well as a single broadband circular polarizer can be achieved.

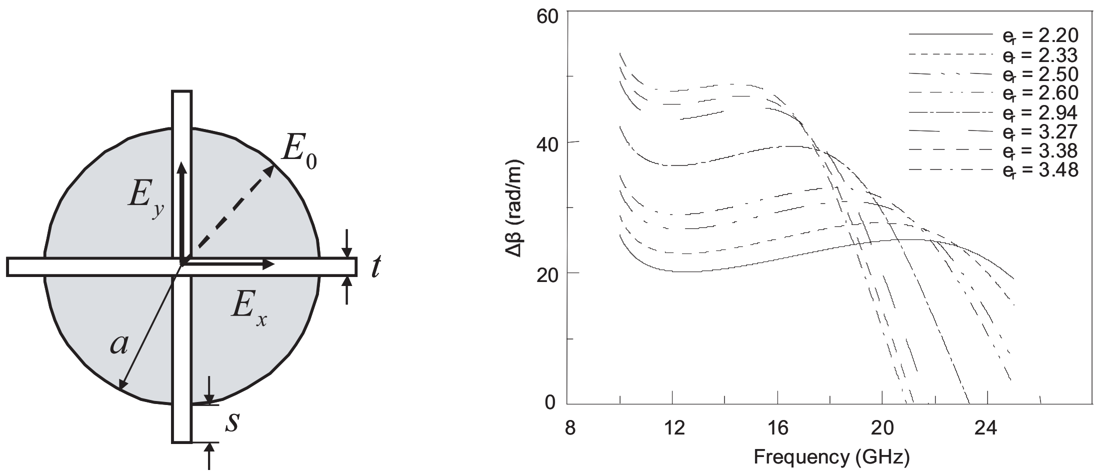

(a) (b)

Figure 2: Field components and propagation constants. (a) Cross-sectional view of the circular polarizer and (b) Propagation constant for various dielectric constant.

Table 1: Specifications and design parameters of the circular polarizers.

Polarizer prototype		**Dual-band**	**Broadband**
Operation band (GHz)		11.7–12.7, 19.7–20.2	11.7–20.2
Septum orientation		Orthogonal	Parallel
Waveguide radius (mm), a		8.7	8.7
Slot dimensions (mm),	s	2.2	2.2
	t	1.57	1.57
Septum lengths (mm),	l_1	207.7	34.9
	l_2	125.7	23.7
Septum materials,	ε_{r1}	2.94	2.2
	ε_{r12}	3.48	2.94

3. Design of Dual-band/broadband Circular Polarizers

Table 1 shows the specifications and the design parameters of the circular polarizers. Waveguide radius is firstly determined by the strategy proposed in [4] to obtain a flatter phase response in the desired frequency ranges. For physical strength and precise location of the dielectric septum, the slot on the waveguide wall can also be determined. Once the cross-sectional dimension of the waveguide is determined, propagation constants with various dielectric septums inserted are then calculated.

To design a dual-band circular polarizer, the prototype shown in Figure 1(a) is utilized. By properly choosing the length and relative dielectric constants of the two septum sections, a 90° and a 270° phase differences can be obtained at the center frequency of the lower and upper operation bands, respectively.

On the other hand, if the second prototype (Figure 1(b)) is used, a single broadband circular polarizer can be designed by properly placing the maximum variation point of phase difference in the desired frequency range. Figure 3 shows the simulation results by Ansoft HFSS for the frequency response of phase difference of the designed dual-band and broadband circular polarizers.

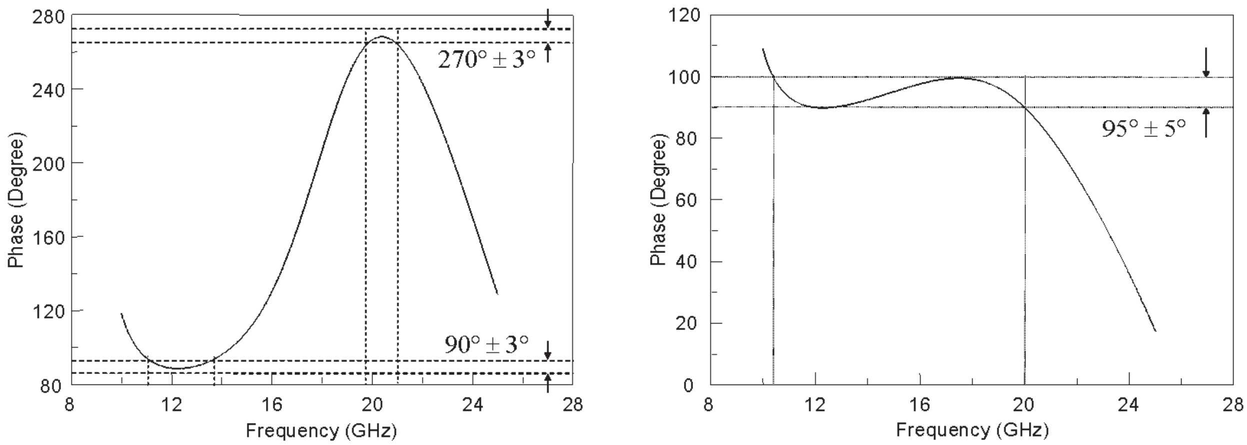

(a) (b)

Figure 3: Phase difference of the polarizers with (a) dual-band and (b) a single broadband responses.

4. Conclusion

Circular polarizers with two cascaded dielectric septum loadings for dual-band and broadband applications are proposed. Simulations results by Ansoft HFSS shows that for the broadband design not only the flatter phase response near the center frequency but also a broader bandwidth are obtained comparing to single section ones [4]. A dual-band design that can never be achieved with single dielectric septum section is also accomplished in this paper. These circular polarizers are currently under fabrication and the measurement results will be presented later in the conference.

Acknowledement

This work was supported in part by the National Science Council, Taiwan, ROC under Grant NSC93-2752-E-002- 003-PAE.

REFERENCES

1. Yoneda, N., M. Miyazaki, H. Matsumura, and M. Yamato, "A design of novel grooved circular waveguide polarizers," *IEEE Trans. Microwave Theory Tech.*, Vol. 48, 2446–2452, Dec. 2000.
2. Bertin, G., B. Piovano, L. Accatino, and M. Mongiardo, "Full-wave design and optimization of circular waveguide polarizers with elliptical irises," *IEEE Trans. Microwave Theory Tech.*, Vol. 50, 1077–1083, Apr. 2002.
3. Chen, M. H. and G. N. Tsandoulas, "A wide-band square-waveguide array polarizer," *IEEE Trans. Antennas Propagat.*, Vol. AP-31, 389–391, May 1973.
4. Wang, S. W., C. H. Chien, C. L. Wang, and R. B. Wu, "A circular polarizer designed with a dielectric septum loading," *IEEE Trans. Microwave Theory Tech.*, Vol. 52, 1719–1723, Jul. 2004.

Mode Transformer between TEM Mode to 1^{st} Higher Mode in Tri-plate Strip Transmission Line

F. Kuroki and K. Miyamoto
Kure National College of Technology, Japan

Printed transmission lines, such as a microstrip transmission line and a coplanar waveguide, are preferable for applications in centimeter-frequencies. They are commonly used in millimeter-wave regions to realize cost-effective front-ends due to good mass-productivity. The printed transmission lines, however, suffer from considerable transmission loss. To reduce such transmission loss, a higher order mode of microstrip transmission line has been studied, but unfortunately, such a mode easily emits unwanted radiation at curved sections and discontinuities.

To realize a low-loss printed transmission line at millimeter-wave frequencies, we developed the first higher mode in a tri-plate strip transmission line. This transmission line, termed higher mode tri-plate strip transmission line (HS line) in this paper, consists of metal strips inserted in a below cutoff parallel plate waveguide as shown in Fig. 1. A basic reactance component such as a slot was investigated to apply to a matching circuit and a suppressor of the lowest mode, which is the TEM mode in the tri-plate strip transmission line. To apply the HS line to some printed strip transmission lines, a mode transformer between the HS line and the tri-plate strip transmission line with only TEM mode propagation was developed. The field distribution of the HS mode in the cross-sectional plane resembles that of the TE_{10} mode in the hollow rectangular metal waveguide, while that of the tri-plate strip transmission line is similar to the coaxial line mode, that is the TEM mode. With this in mind, a mode transformer between the HS line and the tri-plate strip transmission line could be constructed by making a right-angle corner as shown in Fig. 2. To reduce the reflection from the mode transformer, the corner edge was trimmed off. No TEM mode propagation in the HS line is guaranteed by using the TEM mode suppressor consisting of three slots. Fig. 3 shows the measured VSWR from the mode transformer as circles. A flat VSWR performance measured to be 1.6 on average was obtained. To perform perfect matching at 32 GHz, a matching slot was sited behind the TEM mode suppressor as shown in Fig. 2. The VSWR of the mode transformer with the matching slot is plotted in Fig. 3 as dots. It is obvious that there is no reflection, though the center frequency was shifted to 100 MHz. Fig. 4 shows the measured transmission loss versus frequency in the back-to-back structure of two mode transformers, where, to obtain a flat frequency response, the matching slots were not installed. The transmission loss was measured to be less than 0.6 dB in the frequency range from 31 GHz to 33 GHz.

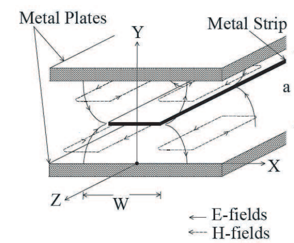

Figure 1: Rough sketch of field distribution of the first higher in tri-plate strip transmission line.

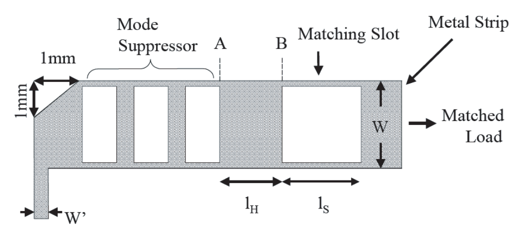

Figure 2: Mode transformer between HS mode and TEM mode.

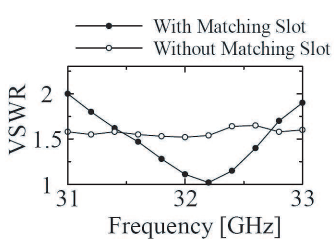

Figure 3: Measured VSWR of mode transformer between HS mode and TEM mode.

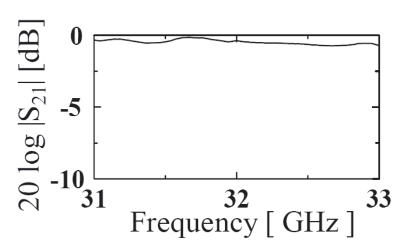

Figure 4: Measured transmission loss versus frequency in back-to-back structure.

High-accuracy Approximation to the Integrated Length of Toroidal/Helical Orbits

R. A. Speciale
Research & Development Inc., USA

Abstract—The new innovative concept of High Power Microwave (HPM) Amplifier recently introduced, combines Multi-Beam Klystron (MBK) and Electron Storage-Ring (ESR) technologies, by using closed, multi-turn Toroidal/Helical electron-orbits. The selected toroidal/helical orbit-configuration was defined as a parametric space-curve in three dimensional space R^3. We get the parametric equations of that orbit. A high-accuracy approximation has now been obtained for the total length of the Toroidal/Helical orbit, that attains much faster numerical computation. Higher accuracy could be attained by using a higher-order expansion of the orbit-length rate-of-increase.

1. Introduction

High power microwave (HPM) sources are almost always designed as vacuum-electronic devices, and are characterized by the capability of generating output powers in the range of Megawatt to Gigawatt, by using beam-voltages of hundreds of kilovolts, and beam-currents of tens of ampere. HPM sources operate in either of three broadly-defined modes: a) Short Pulse, at pulse lengths of 0.1–10 μs, b) Long Pulse, at pulse lengths of 0.1–10 ms, and c) Continuous Wave (CW). The design of high power microwave (HPM) sources has been gradually evolving during at least the past thirty years, primarily stimulated by applications to high energy charged-particle accelerators, and to directed-energy weapons. A number of classic review-papers document that evolution (see [1, 2]). Currently, high energy charged-particle accelerators use almost exclusively high-power klystron amplifiers [3], that attain peak-powers of hundreds of Megawatt in short-pulse operation, tens of Megawatt in long-pulse operation, and about a Megawatt in CW mode. Such amplifiers provide, while converting DC to microwaves, power-efficiency of 50%–60%, and power-gain of 40 dB–60 dB. The electron beam of klystron amplifiers is sharply bunched by *velocity modulation*, followed by a *drift-space* where the accelerated faster electron catch-up with the decelerated slower electron. The so attained sharp bunching generates, upon the continuous-current electron-beam, the required microwave-frequency component, that is the essential source of the generated high-power microwave output.

Quite recently, a number of multi-beam klystrons (MBK) have been developed experimentally, and at least three different MBK models are already commercially available (see [4–8]). Multi-beam klystrons operate at reduced electron-gun voltage, and higher total beam-current than the single-beam designs, thus preventing occasional destructive gun-diode discharges, and increasing the power-efficiency up to $\sim$ 75%. The power-efficiency (measured as the ratio of output microwave power to input DC power) is however still limited, even in MBK, as it is obviously impossible to extract *all* the microwave energy from a sharply-bunched electron-beam, without having the high space-charge-density of the slowing beam force it into uncontrollable defocusing. All high-power klystron amplifiers include therefore a device known as *the beam dump*, which is a high-volume expansion of the klystron vacuum-enclosure, located beyond the microwave-power extraction-structure, where the not-quite completely energy-depleted electron-beam is collected, while converting (*wasting !*) its residual energy to heat *and* X-rays.

2. Toroidal/Helical Orbits

A new, innovative design of High Power Microwave (HPM) Electron-Beam Amplifier was presented by the Author at the PIERS 2004 Symposium, in Pisa, Italy [14]. That new design has the capability of attaining multi-megawatt output power levels, even in long-pulse, high duty cycle or even continuous wave (CW) operation, with very high efficiency, very high spectral-purity, and very low levels of phase and amplitude noise. The new design was initially conceived as a combination of a multi-beam klystron (MBK), with an Electron Storage Ring (ESR). Very high power-efficiency may be attained by having a sharply-bunched High-Current, Relativistic Electron Beam (HIREB) circulate around a *closed*, *re-entrant* multi-turn orbit, within a strong-focusing, alternating-gradient (AG) magnetic field, generated by an azimuth-periodic lattice of beam-guiding magnetic-dipoles, and magnetic quadrupole lenses. High beam currents may then be attained because, by using a multi-turn *helical* electron-beam orbit, running on the outer surface of a virtual torus-surface, the beam current and the space-charge density in each of the individual orbit-turns can be much lower than in a single-turn orbit. That orbit configuration was initially conceived as a way of increasing the power-efficiency of high-power klystron amplifiers, by eliminating *the beam dump*, and by introducing a mechanism of beam-energy recovery, similar to that of Energy-Recovery Linacs (ERL).

It was soon seen however that the use of such closed multi-turn electron-orbit would essentially reduce the foot-print of the newly-conceived device by a factor in the order of the square of the integer number $\boldsymbol{n}$ of turns, while keeping the total orbit length unchanged, relative to that of a single-turn Electron Storage Ring (ESR).

It was also seen that, by keeping the electron-beam energy always in a relativistic range (such as for instance from 50 Mev to 100 Mev), much higher single-turn beam-current, and much higher total stored beam-energy (expressed in Joule) could be attained under a strong-focusing, alternating-gradient (AGS) magnetic field, while at the same time any partial extraction of microwave-energy from the bunched circulating beam would not appreciably change the electron orbital-frequency. Indeed, the total stored beam-energy (expressed in Joule) is obviously stored in the relativistic $(\boldsymbol{\gamma}-1)\,\boldsymbol{m}_0$ mass-increase of the electrons, multiplied by the square of the constant speed of light. Then, by keeping the electron-energy (expressed in Mev) in a relativistic range, very large amounts of microwave energy (expressed in Joule) could be extracted from the circulating sharply-bunched beam, while hardly changing the electron relativistic velocity-factor $\boldsymbol{\beta}$ ($\boldsymbol{\beta} = \sqrt{(\boldsymbol{\gamma}^2-1)/\boldsymbol{\gamma}^2}$, while $\Delta\,\boldsymbol{E} = \Delta\,\gamma \boldsymbol{m}_0 \boldsymbol{c}^2$). As a consequence, such partial microwave-power extraction would hardly change the electron orbit-frequency, provided the beam-energy (expressed in Mev) is kept within a relativistic range, where $\boldsymbol{\beta}$ is a very slow function of $\boldsymbol{\gamma}$. In the light of these considerations, the new HPM amplifier design, that was initially conceived as a combination of the multi-beam klystron (MBK) with an Electron-Storage Ring (ESR), actually appears to perform the function of an Energy-Storage Ring (while still being nevertheless an "ESR"). Quite obviously, in any closed-orbit electron-device, the total orbit length is a parameter of fundamental significance, as it determines both the total electric-charge, and the total beam-energy (expressed in Joule) stored in the orbit, and also determines the orbit-frequency of the electron-bunches. The closed-form exact expression of the orbit-length that was reported in [14], had been obtained by symbolically integrating the rate-of-increase of the orbit-length (also known as "*the speed"!*) as function of the *wrapping-angle* $\boldsymbol{\theta}$, by using *Mathematica*. That expression was however characterized by an extreme degree of complexity, even after being simplified (using the *Mathematica "FullSimplify"* command) from an original a 20-page-long print-out to a single-page expression. The computation-time required by the symbolic integration was only in the order of a minute, even on a modest 166 MHz PC (Dell XPS P166c), but the full simplification of the 20-page-long print-out required four full days, for a total in the order of 96 hours. Even on a modern Workstation, with dual 2.4 GHz Xeon processors (HP xw8000), that simplification requires at least in the order of *six hours*.

3. Orbit Equations

The selected *toroidal/helical* orbit-configuration was defined as a parametric space-curve in three dimensional space R^3, with its Cartesian coordinates being functions of the azimuth-angle $\boldsymbol{\varphi}$ (measured around the torus-axis), and of the *wrapping-angle* $\boldsymbol{\theta}$ (measured around the torus circular cross-section), with the implied condition that the ratio of the two angle periods be rational, such that the orbit closes on itself after an integer number of turns $\boldsymbol{n}$ (for $0 \leq \boldsymbol{\varphi} \leq 2\mathbf{n}\boldsymbol{\pi}$). The parametric equations of that orbit are expressed by:

$$\hat{r}(\varphi,\theta) = x(\varphi,\theta)\cdot\hat{i} + y(\varphi,\theta)\cdot\hat{j} + z(\varphi,\theta)\cdot\hat{k} \tag{1}$$

where $\boldsymbol{\varphi}$ is the azimuth angle around the torus-axis, and $\boldsymbol{\theta}$ is the helical *"wrapping angle"* around the torus circular cross-section. The three Cartesian components $\boldsymbol{x}$, $\boldsymbol{y}$ and $\boldsymbol{z}$ of the position-vector $\boldsymbol{r}$, and the linear relation between the angles $\boldsymbol{\varphi}$, and $\boldsymbol{\theta}$ are given by:

$$x = (R + r\cos\theta)\cos\varphi \tag{2}$$

$$y = (R + r\cos\theta)\sin\varphi \tag{3}$$

$$z = r\sin\theta \tag{4}$$

$$\theta = \frac{n-1}{n}\,\varphi \tag{5}$$

The closed-form, exact expression given in the original paper [14] for the multi-turn electron-orbit length, as function of the azimuth-angle $\boldsymbol{\varphi}$ around the torus-axis, and of the *wrapping-angle* $\boldsymbol{\theta}$, shows a rather daunting degree of complexity, by including all three Elliptic Integrals: a) of the first kind $\mathbf{E}$, b) of the second kind $\mathbf{F}$, and c) of the third kind $\boldsymbol{\Pi}$.

4. Orbit-Length Approximations

A high-accuracy approximation has now been obtained for the total length of the Toroidal/Helical orbit, that attains much faster numerical computation. That approximation was obtained by expanding the orbit-length rate-of-increase $\boldsymbol{ds/d\varphi}$ *("the speed" !)* [13] in powers of the torus aspect-ratio $\boldsymbol{c = r\ /\ R}$, and by integrating that expansion term-by-term. The $\mathbf{6}^{th}$-order power-expansion of the orbit-length rate-of-increase obtained is expressed by:

$$\begin{aligned}\frac{d\,s}{d\,\varphi} &= R\sqrt{(1\,+\,c\cos\theta)^2\,+\,c^2\left(\frac{n\,-\,1}{n}\right)^2}\\ &\cong\ w_0\,+\,w_1\,c\,+\,w_2\,c^2\,+\,w_3\,c^3\,+\,w_4\,c^4\,+\,w_5\,c^5\,+\,w_6\,c^6\end{aligned}\tag{6}$$

where the seven $\boldsymbol{w}_i$ expansion-coefficients are given by:

$$w_0 = R \tag{7}$$

$$w_1 = R\cos\theta \tag{8}$$

$$w_2 = \frac{1}{2}\,R\left(\frac{n\,-\,1}{n}\right)^2 \tag{9}$$

$$w_3 = -\frac{1}{2}\,R\left(\frac{n\,-\,1}{n}\right)^2\cos\theta \tag{10}$$

$$w_4 = \frac{R}{8\,n^2}\left(\frac{n\,-\,1}{n}\right)^2\left[4\,n^2\cos^2\theta\,-\,(n\,-\,1)^2\right] \tag{11}$$

$$w_5 = -\frac{R}{8\,n^2}\left(\frac{n\,-\,1}{n}\right)^2\cos\theta\,\left[3\,(2\,n\,-\,1)\,-\,n^2\,\left(3\,-\,4\,\cos^2\theta\right)\right] \tag{12}$$

$$w_6 = \frac{R}{16}\left(\frac{n\,-\,1}{n}\right)^2\left\{\left[\left(\frac{n\,-\,1}{n}\right)^2-\,6\,\cos^2\theta\right]^2-\,28\,\cos^4\theta\right\} \tag{13}$$

where the *wrapping-angle* $\boldsymbol{\theta}$ is related to $\boldsymbol{\varphi}$ through the linear, rational relation (5): $\boldsymbol{\theta}\ =\ [\,(n-1\,)\,/n]\ \boldsymbol{\varphi}$.

Preliminary numerical computations, using $\boldsymbol{n} = 9$ and $\boldsymbol{c} = 0.2$, have shown the residual error of the $\mathbf{6}^{th}$-order expansion of the orbit-length rate-of-increase given in (6) to have a residual error of $-\mathbf{4}\cdot\mathbf{10}^{-6}$ to $+\,\mathbf{3}\cdot\mathbf{10}^{-6}$ across the $0\ \leq\ \boldsymbol{\theta}\ \leq\ 2\boldsymbol{\pi}$ range, that is consistently periodic across the whole $\mathbf{0}\ \leq\ \boldsymbol{\theta}\ \leq\ (\boldsymbol{n}-\ \mathbf{1})\ \mathbf{2}\boldsymbol{\pi}$ range (Figure 1).

The orbit-length approximate expression, resulting from a term-by-term integration of the $\mathbf{6}^{th}$-order expansion (6) , includes five terms, and is expressed by:

$$s\,(\varphi) = h_1\,\theta\,+\,h_2\,\sin\theta\,+\,h_3\,\sin 2\,\theta\,+\,h_4\,\sin 3\,\theta\,+\,h_5\,\sin 4\,\theta \tag{14}$$

where the five $\boldsymbol{h}_i$ coefficients are functions of the torus aspect-ratio $\boldsymbol{c = r\ /\ R}$, and of the number of orbit-turns $\boldsymbol{n}$:

$$h_1 = R\left\{1{+}\frac{1}{2}\left(\frac{n{-}1}{n}\right)^2c^2{+}\frac{1}{4}\left(\frac{n{-}1}{n}\right)^2\left[1{-}\frac{1}{2}\left(\frac{n{-}1}{n}\right)^2\right]c^4{-}\frac{1}{16}\left(\frac{n-1}{n}\right)^2\left[2\left(\frac{n-1}{n}\right)^4{-}3\frac{(2n-1)^2}{n^4}\right]c^6\right\} \tag{15}$$

$$h_2 = R\left[1-\frac{1}{2}\left(\frac{n-1}{n}\right)^2c^2-\frac{3}{8n^2}\left(\frac{n-1}{n}\right)^2(2n-1)\,c^4\right]c \tag{16}$$

$$h_3 = R\,\frac{1}{16\,n^2}\left(\frac{n\,-\,1}{n}\right)^2\left[\left(2\,-\,c^2\right)\,n^2\,+\,3\,c^2\,(2\,n\,-\,1)\right]\,c^4 \tag{17}$$

$$h_4 = -R\frac{1}{24}\left(\frac{n-1}{n}\right)^2c^5 \tag{18}$$

$$h_5 = R\frac{1}{64}\left(\frac{n-1}{n}\right)^2c^6 \tag{19}$$

The graphic displays of the integrated rate-of-increase $\mathbf{6}^{th}$-order power expansion shown in Figure 2 have been computed for Toroidal/Helical orbits with $\boldsymbol{n}\ =\ 9$ turns, and aspect-ratio $\boldsymbol{c\ =\ r\ /\ R}$ from 0.1 to 0.4, in steps of 0.1.

A preliminary numerical comparison of the approximate orbit-length expression given in Equation (14), computed using $\boldsymbol{n}\ =\ 9$ and $\boldsymbol{c}\ =\ 0.2$, has shown the residual error of the approximation to be in the order of

$\pm$ $\mathbf{3} \cdot \mathbf{10}^{-6}$, with a single oscillation period for $\mathbf{0} \leq \boldsymbol{\theta} \leq 2\boldsymbol{\pi}$ (Figure 3). The residual error appears to be a periodic function of the *wrapping-angle* $\boldsymbol{\theta}$, through the whole interval $\mathbf{0} \leq \boldsymbol{\theta} \leq (\mathbf{n}-\mathbf{1})2\boldsymbol{\pi}$. While the orbit-length exact-expression given in [14] shows, for these parameter-values, a periodic discontinuity jump of -6.3836527 at $\boldsymbol{\theta}$-values that are odd-multiples of $\boldsymbol{\pi}$, the approximation given in Equation (14) is completely continuous, and monotonic across the whole $\mathbf{0} \leq \boldsymbol{\theta} \leq (\mathbf{n}-\mathbf{1})2\boldsymbol{\pi}$ range, and its computational speed is quite conveniently substantially higher, thus providing the possibility of determining the electron orbital-period, around either a single-turn or an $\boldsymbol{n}$-turn Toroidal/Helical orbit (Figure 3). Quite obviously, higher accuracy could be attained by using a higher-order expansion of the orbit-length rate-of-increase.

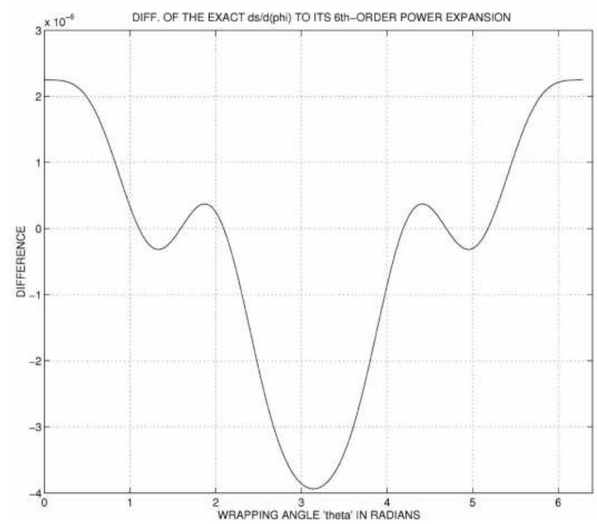

Figure 1: Residual error of the 6th-order expansion of the orbit-length rate-of-increase.

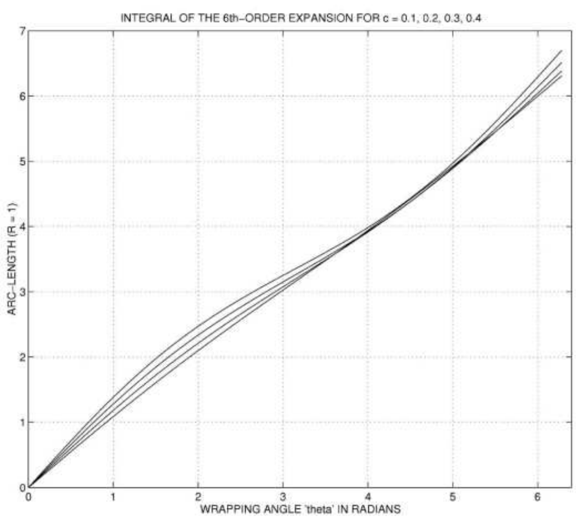

Figure 2: Integrated 6^{th}-order expansion of the toroidal/helical orbit-length rate-of-increase.

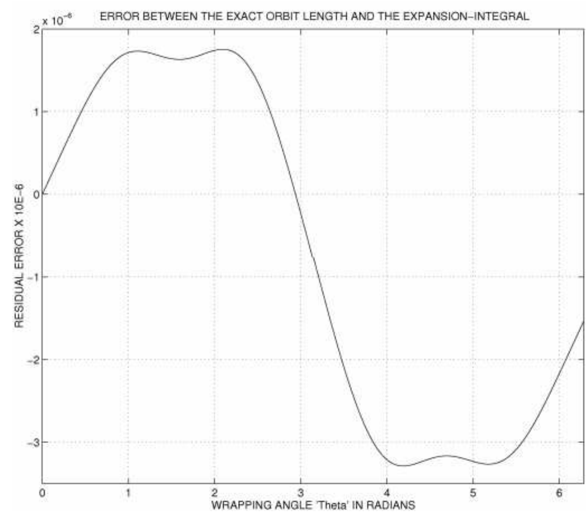

Figure 3: Residual error of the 6^{th}-order power-expansion integral s(φ).

5. Energy Storage

A tentative baseline design of an HPM amplifier as described in [14], has been generated, attempting to match the 1.3 GHz TESLA-Klystron specifications [15]. The virtual torus-surface radii computed are $\boldsymbol{R}$ = 1444.99 mm, and respectively $\boldsymbol{r}$ = 288.998 mm, while the torus median-circle circumference is $\boldsymbol{L}_c$ = 9079.15 mm.

The total 9-turn orbit-length computed $\boldsymbol{L}_t$ = 83.019 m shows the use of a $\boldsymbol{n}$-turn Toroidal/Helical orbit to lead to a very compact *"device"* having a surface foot-print $\boldsymbol{n}^2$ times (= 81!) less than a conventional, circular-orbit, electron-storage-ring *"tunnel-installation"*. Further, it appears feasible to have a total of 120 electron-bunch, in 40 sets of three bunch each, nominally spaced by an azimuth increment $\Delta\boldsymbol{\varphi} = 9^o$ around the torus median-circle circumference, so that the bunch-set cyclotron-frequency is only $\boldsymbol{f}_c$ = 1.3 GHz/40 = 0.0325 GHz $\equiv$ 32.5 MHz, corresponding to an electron cyclotron period $\boldsymbol{t}_c$ = 30.7692 nanosec. The three electron-bunch in each set are then spaced by a nominal wrapping-angle increment $\Delta\theta = 120^o$. Also, the orbit-parameters $\boldsymbol{R}$, $\boldsymbol{r}$, $\boldsymbol{L}_c$, and $\boldsymbol{L}_t$ would hardly change if the electron-energy is always kept sufficiently high, such as from 50 Mev to 150 Mev. Further, it appears also feasible to run a total average beam-current of 9 orbit-turn $\times$ 1.11 kA each = 10 kA total, attaining a circulating electron-beam power of 500–1500 Gw, and a total beam kinetic-energy content between $\boldsymbol{E}_1$ = 500 $\boldsymbol{t}_c$ = 15,384.615 Joule at 50 Mev, and $\boldsymbol{E}_2$ = 1500 $\boldsymbol{t}_c$ = 46,153.385 Joule at 150 Mev. Extracting a partial energy $\Delta\mathbf{E} = \boldsymbol{E}_2 - \boldsymbol{E}_1 = 30{,}769$ Joule, by switching the circulating electron-beam from an accelerating-structure to a microwave-power extraction-structure, would be sufficient to generate a 10 Mw peak-power, 3 msec long microwave pulse, thus exceeding the required TESLA-Collider RF System specification [15] by a factor two in pulse-length. Re-acceleration of the electron-beam could be performed during the pulse-to-pulse 98.5 ms spacing, of the specified maximum 10 Hz pulse-repetition rate. The re-acceleration could be performed at the third sub-harmonic of the required 1.3 GHz output-frequency, by placing the re-acceleration structure along a single orbit-turn, where the azimuth bunch-spacing is $\Delta\boldsymbol{\varphi} = 27^o$.

6. Conclusion

We give an overview on the design of high power microwave (HPM) sources. As a new, innovative design of High Power Microwave (HPM) Electron-Beam Amplifier was presented not long before, a high-accuracy approximation has now been obtained for the total length of the Toroidal/Helical orbit, that attains much faster numerical computation. Higher accuracy could be attained by using a higher-order expansion of the orbit-length rate-of-increase. A tentative baseline design of an HPM amplifier has been generated, attempting to match the 1.3 GHz TESLA-Klystron specifications.

REFERENCES

1. Gold, S. H. and G. S. Nusinovich, "Review of high-power microwave source research," *Rev. Sci. Instrum.*, Vol. 68, No. 11, 3945–3974, November 1997. http://www.ireap.umd.edu/ireap/personnel/publications/RSI 03945.pdf
2. Wilson, P. B., "Development and advances in conventional high power rf systems," SLAC-PUB-95-6957, Stanford Linear Accelerator Center, Stanford University, Stanford, CA 94309 USA, http://www.slac.stanford.edu/cgi-wrap/getdoc/slac-pub-6957.pdf.
3. Caryotakis, G., "The klystron: a microwave source of surprising range and endurance," *Phys. Plasmas*, Vol. 5, No. 5, 1590–1598, May 1998. http://www.slac.stanford.edu/cgi-wrap/getdoc/slac-pub-7731.pdf; http://www.slac.stanford.edu/ cgi-wrap/getdoc/slac-pub-8186.ps.gz; http://www.eece.unm.edu/ifis/papers/MTT.pdf; http://media.wiley.com/*product_data*/excerpt/60/07803600/0780360060.pdf; http://www-project.slac.stanford.edu/ lc/wkshp/snowmass2001/snow/Ch4.pdf.
4. Yano, S. and S. Miyake, "The toshiba E3736 multi-beam klystron," *Proceedings of LINAC 2004*, Lübeck, Germany, Paper THP45, 706–708.
5. Beunas, A., G. Faillon, S. Choroba. S., and A. Gamp, "A high efficiency long pulse multi beam klystron for the tesla linear collider," http://www.cap.bnl.gov/mumu/studyii/ $final\_draft$/chapter-14/chapter-14.pdf.
6. Larionov, A., V. Teryaev, S. Matsumoto, and Y. H. Chin, "Design of multi-beam klystron in X-band," *Proceeding of the 27th Linear Accelerator Meeting in Japan*, IEDM, 1986A, 2002. http://lcdev.kek.jp/Conf /LAM27/8P-13.pdf or: http://lcdev.kek.jp/USJ/Paper.JFY98-02.pdf
7. Larionov, A., "Optical system of the powerful multiple beam L-band klystron for linear collider," *Proceedings of RuPAC XIX*, 456–458, Dubna 2004.
8. Jongewaard, E., G. Caryotakis, C. Pearson, R. M. Phillips, D. Spren, and A. Vlieks, "The next linear collider klystron deverlopment program," *XX International Linac Conference*, Monterey, California, Paper THA03, 739–741.
9. Rees, D., "Design of 250-MW CW RF system for APT," 0-7803-4376-X/98/, *IEEE*, 2889–2893, 1998. http://epaper.kek.jp/pac97/papers/pdf/9C003.PDF
10. Rees, D., W. Roybal, and III. J. Bradley, "Collector failures on 350 MHz, 1.2 MW CW lystrons at the low energy demonstration accelerator (LEDA)," *XX International Linac Conference*, Monterey, California, Paper THE12, 998–1000.
11. Dodson, C. T. J., "Mathematics 117: lecture notes for curves and surfaces module," *Department of Mathematics, UMIST*, 1–13, Expressions (28) and (29) at page 6, http://www.ma.umist.ac.uk/kd/ma117/117ln.pdf.
12. Dodson, C. T. J., "Introducing curves," *Department of Mathematics, UMIST*, 1–11, Expressions (25) and (26) at page 9, http://www..ma.umist.ac.uk/kd/curves/curves.pdf.
13. Dodson, C. T. J., "Mathematics 117: lecture notes for curves and surfaces module," *Department of Mathematics, UMIST*, 1–13, Expressions (3) at page 3, http://www.ma.umist.ac.uk/kd/ma117/117ln.pdf.
14. Speciale, R. A. "High power microwave amplifiers with toroidal/helical orbits," *PIERS 2004*, Pisa, Italy.
15. Choroba, S., "The tesla RF system," RF 2003, 2003.

Multilevel Modified Nodal/Multiport State-space Approach for Frequency-domain Simulation of Large-scale Nonlinear RF and Microwave Circuits

O. P. Paixão and H. E. Hernández-Figueroa
Universidade Estadual de Campinas, Brazil

A multilevel approach for frequency-domain simulation of large-scale nonlinear RF and microwave circuits, including the presence of noise and thermal effects, is presented. In this approach, the circuit to be simulated is firstly decomposed into hierarchically interconnected supernetworks represented by a nodal equation [1]. Then, for each supernetwork we apply a piecewise network decomposition that separates it into linear and nonlinear subnetworks [2]. The nonlinear subnetwork encompasses all nonlinear devices (e.g., FETs and HBTs) in the supernetwork and it is formulated by an extended multiport state-space analysis (MSSA) [3]. While the embedding linear subnetwork is formulated using the classical modified nodal analysis (MNA) [4].

The advantages of using the extended MSSA instead of MNA for formulating the nonlinear subtnetwork is twofold: (i) it uses one single variable to represent a nonlinear function controlling voltage and, (ii) it naturally separates the nonlinear (controlled sources) equations from the other set of linear equations, namely differential (lumped memory elements), difference (distributed and delay elements) and additional (controlled sources) equations. Nevertheless, the MNA is a very powerful technique for formulating the linear subnetwork. It is well conditioned and structured and, it can be efficiently solved via LU factorization combined with sparse matrix computations. The MSSA uses a simple table-based methodology in order to generate the nonlinear subnetwork equations. It worth pointing out, that a very small matrix inversion is required for eliminating the linear (differential, difference and additional) equations and associated linear state-variables.

Our state-space approach is more efficient than the widely used parametric state-space approach [5], since the later approach may lead to a non-square system of equations and may involve high-order derivatives of nonlinear state-variables. These high-order derivatives leads to cumbersome expressions for the computation of nonlinear functions sensitivities with respect to the state-variables.

Finally, we describe the application of the above theory to the following RF and microwave circuit problems: nonlinear steady-state analysis via harmonic balance [5], large-signal conversion signal and noise analysis, and small-signal multiport hybrid signal and noise correlation matrix analysis [6]. New formulae for conversion from multiport hybrid parameters to multiport scattering parameter representation, and vice-versa, are included. Finally, we present frequency-domain simulation results for GaAs MESFET microwave power amplifier and InP HBT millimeter-wave downconverter. These results, obtained by our in-house software, validate the theory presented herein.

REFERENCES

1. Zhang, X., R. H. Byrd, and R. B. Schnabel, "Parallel methods for solving nonlinear block bordered systems of equations," *SIAM J. Sci. Stat. Comput.*, Vol. 13, No. 4, 841–859, July 1992.
2. Nakhla, M. S. and J. Vlach, "A piecewise harmonic balance technique for determination of periodic response of nonlinear systems," *IEEE Trans. Circuits Syst.*, Vol. 23, No. 2, 85–91, Feb. 1976.
3. Sobhy, M. I., E. A. Hosny, and M. A. Nassef, "Multiport approach for the analysis of microwave nonlinear networks," *Int. J. Num. Modelling: Electronic Net., Dev. Fields*, Vol. 6, 67–81, 1993.
4. Ho, C., A. E. Ruehli, and P. A. Brennan, "The modified nodal approach to network analysis," *IEEE Trans. Circuits Syst.*, Vol. 22, No. 6, 504–509, June 1975.
5. Rizzoli, V., et al., "State-of-the-art harmonic balance simulation of forced nonlinear microwave circuits by the piecewise technique," *IEEE Trans. Microwave Theory Tech.*, Vol. 40, No. 1, 12–28, Jan. 1992.
6. Russer, P. and S. Müller, "Noise analysis of linear microwave circuits," *Int. J. Num. Modelling: Electronic Net., Dev. Fields*, Vol. 3, 287–316, 1990.

Low Cost 60 GHz Gb/s Radio Development

S. Pinel, **C.-H. Lee**, **S. Sarkar**, **B. Perumana**
S. Padvanama, **R. Mukhopadhyay**, **and J. Laskar**
Georgia Institute of Technology, USA

Abstract—The recent advances of CMOS and SiGe process technologies have now made the design of low-cost highly integrated millimeter-wave radios possible in Silicon. In combination with an optimum organic Liquid Crystal Polymer packaging approach, this represents a unique opportunity to develop Gb/s radio that could address the increasing demand in term of data rate throughput of the emerging broadband wireless communication systems. In this paper we discuss the circuit and module challenges that will enable a successful deployment of 60 GHz gigabits wireless systems.

1. Introduction

The demand for ultra-high data rate wireless communication systems is increasing daily with the emergence of a multitude of multimedia applications. In particular, the needs become urgent for ultrahigh speed personal area networking and point-to-point or point-to-multipoint data link. This demand has since pushed the development of technologies and systems operating at the millimeter-wave frequencies, and overcome the current limitations of alternative solution such as 802.11n and UWB. This trend has also been reinforced by the exponentially growth of the emerging automotive collision avoidance radar applications. Indeed, the availability of several GHz band-width unlicensed ISM bands in the 60 GHz spectrum represents a great opportunity for ultra-high speed short-range wireless communications [1]. Since the mid–90's, many examples of MMIC chip-set have been reported for 60 GHz radio applications using GaAs FET and InP pHEMT technologies [2]. Despite their commercial availability and their outstanding performances, these technologies struggle to enter the market because of their prohibitive cost and their limited capability to integrated advanced base-band processing. In addition, the combination, of a low cost highly producible module technology, featuring low loss and embedded function such as antenna, is required to enable a high volume commercial use of the 60 GHz systems.

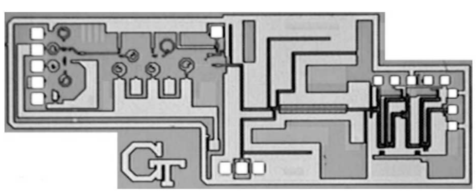

Figure 1: Photo of SiGe 60 GHz integrated MMIC.

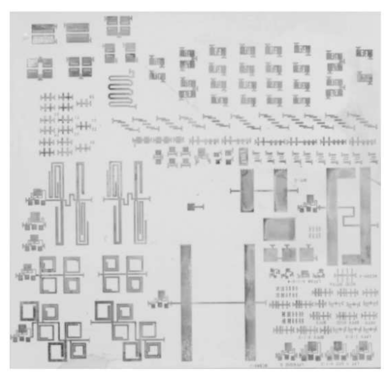

Figure 2: Photo of fabricated LCP substrate.

2. Device Technology

In this paper, we will present and discuss the advances of CMOS and SiGe technology has advanced to enable a complete chipset for 60 GHz applications [4–6]. The front-end architecture using a sub-harmonic approach will be detailed and analyzed and example of circuits such as millimeter-waves LNA, mixer and VCO will be presented. An example of integrated front-end chip that has been developed for this application is shown in Figure 1. It includes a 30 GHz cross-coupled VCO oscillating at a center frequency of 30.1 GHz and exhibiting 2.3 GHz tuning range. The maximum output power after buffer is around -11.7 dBm at 29.54GHz. The sub-harmonic APDP mixer has a measured minimum down-conversion loss of 8.3 dB with a greater than 4 GHz of single-sided 3-dB baseband bandwidth with a 5.5 dBm local oscillator signal at 30.5 GHz. An input 1dB compression point of -7dBm has been recorded. This is the first report of a 60 GHz sub-harmonic mixer on SiGe processes that can be applicable to multi-gigabit wireless personal area network application. A single stage cascode LNA has been measured to have about 15dB of gain. A 2 stages cascode LNA is under development to be combined with the others building blocks.

3. Module Technology

At last, the packaging of the 60 GHz radio represents a major challenge. The Liquid Crystal Polymer has emerged as a promising low-cost alternative for millimeter-wave module implementation [7]. It combines uniquely outstanding microwave performances, low cost and large area processing capability. It appears as a platform of choice for the packaging of the future 60 GHz gigabit radio. We will present the recent advances in developing mmW functions on LCP substrate such as filter and antennas as shown in Figure 2. The optimum combination and co-design of these technologies (Figure 1) is the key for the successful deployment of ultra-high speed, high capacity, 60 GHz WLAN access for very dense urban network and hot spot coverage. Many other commercial applications will directly benefit from this advance. This includes high data rate Wireless Multimedia Access, compact Wireless Gigabit Ethernet and Wireless FireWire/IEEE–1394 link that can be ultimately combined with a fiber or cable backhaul network.

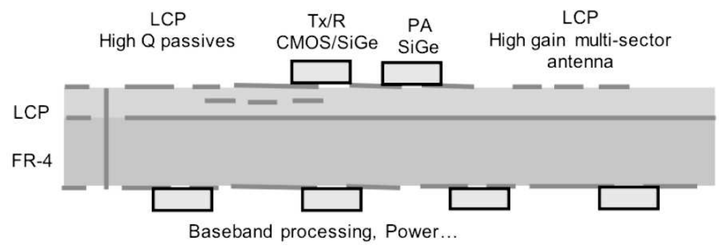

Figure 3: Concept view of a 60 GHz Gb/s radio module.

4. Conclusion

We discussed in this paper the circuit and module challenges for the next generation gigabits radio operating at 60 GHz. We highlighted the technology issues and choices based on application, system architecture, circuit and packaging considerations. The recent advances of CMOS and SiGe process technologies have now made the design of low-cost, highly integrated millimeter-wave radios possible in Silicon. In combination with an optimum packaging approach, such as a Liquid Crystal Polymer platform, these advances could have a major impact on the cost and the performances of the future high speed systems and lead a to a successful deployment of the 60 GHz gigabit wireless radio.

REFERENCES

1. Smulders, P., "Exploiting the 60 GHz band for local wireless multimedia access: prospects and future directions," *Communications Magazine, IEEE,* Vol. 40, Issue: 1, 140–147, Jan. 2002.
2. Ohata, K., et al., "Wireless 1.25 Gb/s transceiver modules utilizing multilayer co-fired ceramic technology," *ISSCC Digest*, 7–9, Feb. 2000.
3. Jagannathan, B., et al., "Self aligned SiGe NPN transistors with 285 GHz fmax and 207 GHz Ft in a manufacturable technology," *IEEE Electron Device Letters*, Vol. 23, 258–260, Issue: 5, May 2002.
4. Reynolds, S. K., B. A. Floyd, and T. Zwick, "60 GHz transceiver circuits in SiGe bipolar technology," *IEEE ISSCC Dig. Tech. Papers,* 442–443, Feb. 2004.
5. Ferndahl, M., H. Zirath, et al., "CMOS MMICs for microwave and millimeter wave applications," *Microwaves, Radar and Wireless Communications*, *MIKON-2004. 15th*, *International Conference on*, Vol. 1, No. 17–19, 247–248, May 2004.
6. Winkler, W., J. Borngraber, B. Heinemann, and P. Weger, "60 GHz and 76 GHz oscillators in 0.25/spl mu/m SiGe:C BiCMOS," *Solid-State Circuits Conference*, *Digest of Technical Papers. ISSCC*, *2003 IEEE International*, 454–507, 2003.
7. Tentzeris, M. M., J. Laskar, J. Papapolymerou, S. Pinel, V. Palazzari, R. Li, G. de Jean, N. Papageorgiou, D. Thompson, R. Bairavasubramanian, S. Sarkar, and J.-H. Lee, "3-D-integrated RF and millimeter-wave functions and modules using liquid crystal polymer (LCP) system-on-package technology," *IEEE Transactions on Advanced Packaging and Manufacturing Technology,* Vol. 27, 332–340, Issue: 2, May 2004.